Enhanced heating rate of black carbon above planetary boundary layer over megacities in summertime

Dantong Liu[1,3], Delong Zhao[2,3,6], Zhenzhen Xie[4], Chenjie Yu[7], Ying Chen[8], Ping Tian[2,3], Shuo Ding[1], Kang Hu[1], Douglas Lowe[7], Quan Liu[2,3], Wei Zhou[2,3], Fei Wang[2,3], Jiujiang Sheng[2,3], Shaofei Kong[5], Dawei Hu[7], Zhenzhu Wang[9], Deping Ding[2,3]

[1]Department of Atmospheric Sciences, School of Earth Sciences, Zhejiang University, Hangzhou, Zhejiang, China

[2]Beijing Weather Modification Office, Beijing, China

[3]Beijing Key Laboratory of Cloud, Precipitation and Atmospheric Water Resources, Beijing, China

[4] Huaian Meteorological Observatory of Jiangsu Province, Huaian, China

[5]Department of Atmospheric Sciences, School of Environmental Studies, China University of Geosciences (Wuhan), Wuhan, China

[6]School of Atmospheric Sciences, Nanjing University, Nanjing, China

[7]Centre for Atmospheric Sciences, School of Earth and Environmental Sciences, University of Manchester, Manchester M13 9PL, UK

[8]Lancaster Environment Centre, Lancaster University, Lancaster LA1 4YQ, UK

[9]Anhui Institute of Optics and Fine Mechanics, Chinese Academy of Sciences, Hefei, 230031, Anhui, China

Abstract

The fast development of a secondary aerosol layer was observed over megacities in eastern Asia during summertime. Within three hours, from midday to early afternoon, the contribution of secondary aerosols above the planetary boundary layer (PBL) increased by a factor of 3-5, and the coatings on the black carbon (BC) also increased and enhanced its absorption efficiency by 50%. This tended to result from the intensive actinic flux received above the PBL which promoted the photochemical reactions. The absorption of BC could be further amplified by the strong reflection of solar radiation over the cloud top across the PBL. This enhanced heating effect of BC introduced by combined processes (intensive solar radiation, secondary formation and cloud reflection) may considerably increase the temperature inversion above the PBL. This mechanism should be considered when evaluating the radiative impact of BC, especially for the polluted regions receiving strong solar radiation.

Key words: Black carbon, absorption enhancement, heating rate, cloud reflection

1. Background

The absorption of shortwave radiation, and consequential atmospheric heating effect, by black carbon (BC) has important impacts on the atmospheric radiative balance (Ramanathan and Carmichael, 2008). In regions with high BC emissions, these climatic effects may be intensified by its strong lower atmosphere heating and surface dimming effect, which could alter the thermodynamic structure of the planetary boundary layer (PBL) (Babu et al., 2002; Ding et al., 2016). The absorption efficiency of BC, described as the absorption coefficient per unit mass of refractory BC (rBC), will be enhanced if coated with non-BC materials, through the lensing effect (Liu et al., 2017). In addition, the heating effect will depend on the actinic flux incidental on the BC particles, which could be significantly increased at higher altitudes, because less dimming will be caused by aerosol optical depth (Norris and Wild, 2009).

It has been demonstrated in modelling studies that the absorption capacity of BC depends considerably on the location of the BC layer relative to the cloud layer, e.g. the absorption will be significantly enhanced if BC layer is above the cloud layer due to strong reflection by cloud top, whereas below the cloud layer the dimming effect will reduce the solar flux deposited on the BC (Jacobson, 2012; Nenes et al., 2002). The position of the BC layer relative to cloud could be crucial to determine its impact on cloud microphysics by heating at different levels (Johnson et al., 2004; Koch and Del Genio, 2010). This study presents the aircraft in-situ measurements, including the full aerosol size distribution and BC size-resolved mixing state, throughout the PBL (containing cloud layers) and lower atmosphere over a megacity in eastern China during summertime. The measurements of vertical profiles were conducted during different times of the day to reveal the diurnal evolution of the heating impact of BC.

2. Measurements and data analysis

2.1 Instrumentation and Data Processing

The aircraft KingAir-350 was deployed (Liu et al., 2018) to conduct vertical profiles over three successive days in summertime (13th to 15th of July, 2018) over the Xuzhou megacity in Eastern China (Fig. 1a). Each flight will be referred to by the date (0713, 0714, and 0715) from now on. The meteorological parameters, including ambient pressure, temperature, relative humidity and wind speed/direction, were characterized in-situ by the AIMMS-20 (Aircraft Integrated Meteorological Measurement System, Aventech Research Inc), which was calibrated on an annual basis. The typical

aircraft speed was about 250 km h^{-1}, and the ascent and descent rates during profiles were ~2–5 ms^{-1}. As shown in Fig. 1b, the morning (9am) and midday (11:30am) profiles were performed on 0713, while the midday (12:00pm) and early afternoon (14:00pm) profiles were on 0714 and 0715. Night flights were also performed on all three days. The profiles covered the time of the day receiving the most intensive solar radiation across the midday. HYSPLIT backtrajectory analysis (Draxler and Hess, 1998) (Fig. 1a) using 1º ×1º, 3-hourly GDAS1 reanalysis meteorology, was performed to track the airmass histories for all profiles. Two more flight campaigns conduced over Beijing in 2016 winter and 2012 summer (Fig. 1b) are introduced (Zhao et al., 2019) to only support the phenomenon observed here but the detailed radiative transfer calculation is not performed.

A wing-mounted Passive Cavity Aerosol Spectrometer Probe (PCASP-100X, DMT Inc, USA) was used to measure the particle size distribution at diameter=0.12-2.5μm, at a time resolution of 1s. A wired heater on top of the inlet, and the dry sheath flow, assured the particles measured by the PCASP were in a dry state, with RH < 40% (Strapp et al., 1992). In addition, the aerosol inlet of the aircraft included a silicate dryer, so aerosol measurements inside the cabin were also dry. The particulate matter (PM1) used in this study is derived from the PCASP optically measured size distribution by assuming an average density of 1.5 g m^{-3} (Cross et al., 2007). The Aitken and accumulation mode particle at diameter=6-520nm was measured by an Engine Exhaust Particle Sizer (EPS, TSI inc.) with time resolution of 1s. The aerosol scattering cross section (C_{sca}) and asymmetry parameter (g) for each size bin is calculated based on the PCASP-measured size distribution by assuming a refractive index 1.50+0i. A fast cloud droplet probe (FCDP, SPEC inc.) (O'Connor et al., 2008) was used to measure the droplet size distribution at ambient RH. All of the aerosol data in cloud was screened out, based on the FCDP measured liquid water content (LWC) >0.001g m^{-3}, but the LWC is used to indicate the location of cloud layers.

The physical properties of BC were characterized by a single particle soot photometer (SP2, DMT inc.) (Schwarz et al., 2006; Zhao et al., 2015). The SP2 is able to measure the rBC mass and associated coating for each rBC-containing particle. The BC core size is measured at 0.05-0.45μm and the remaining mass outside of the detectable range is obtained by a lognormal extrapolation (Fig. S4). As the actual coating thickness depends on both the rBC core and coated BC size, a metric of coating information in bulk, described as a mass ratio of coating/rBC, is used to represent the overall coating status of the particle ensemble during a given time period (Liu et al., 2014). Recent work shows this metric is able to represent the total mass of coatings associated with BC (Ting et al., 2018). The absorption cross section (C_{abs}, in m^2) or C_{abs} normalized by rBC mass (MAC, in m^2g^{-1}) could be calculated based on measured rBC core size-resolved mixing state (an example given in Fig. S10b)

via core-shell mixing rule using BC refractive index of 1.95-0.79i (Bond and Bergstrom, 2006) and coating refractive index of 1.50-0i (Liu et al., 2015).

Fig. S5 shows an example of all size distributions measured on 0714. The scattering coefficient (σ_{sca}) is obtained by integrating the number concentration (*N(D)*) and C_{sca} for all PCASP bins; and the absorption coefficient (σ_{abs}) is the integration of C_{abs} and BC number concentration $N(D_c)$ for all SP2 BC core size bins (D_c up to 0.6μm will include >95% of the total rBC mass in this study). The sum of both gives the extinction coefficient, as expressed in Equation (1):

$$\sigma_{ext} = \sigma_{sca} + \sigma_{abs} = \int_{D=0.12um}^{2um} N(D)C_{sca}(D)dD + \int_{D_c=0.08um}^{0.60um} N(D_c)C_{abs}(D_c)dD_c \qquad (1).$$

This calculation is performed for every 200m altitude bin using the mean PCASP size distribution. The single scattering albedo (SSA=$\sigma_{sca}/\sigma_{ext}$) and asymmetry parameter (g) are also obtained for each altitude bin. The aerosol optical depth - AOD(h) for each altitude bin (h) is obtained from the altitude-integrated $\sigma_{ext}(h)$, as expressed in Equation (2):

$$AOD(h) = \sigma_{ext}(h)\Delta h \qquad (2).$$

The AOD, SSA and g as a function of altitude (Fig. S8) serve as inputs for the radiative transfer calculation given below.

Micro-pulse lidars at 532nm (MPL-4B, Sigmaspace Co., USA), were located at Huaian and Hefei (marked as black dots in Fig. 1a) to monitor the temporal evolution of aerosol layer. A Wind-Profile-Radar (Airda-3000, Airda Co., China) was located close to Xuzhou (34.402ºN,118.017ºE) to measure wind profiles.

2.2 Calculation of BC absorption and heating rate

The actinic flux spectrum (λ=250-2550nm) was calculated using the pseudo-spherical version of the Discrete Ordinates Radiative Transfer Code (DISORT), as implemented in the libRadtran software package (Emde et al., 2016). In this study, the aerosol AOD, SSA and g used are the in-situ measured parameters based on the PCASP and SP2 measurements (see above) and calculated at each λ. The λ-dependent AOD is derived from the calculation based on the PCASP measurement, which is used as an input, expressed as:

$$AOD(\lambda)/AOD(870)=0.16+20.6*\exp(-0.0037*\lambda) \qquad (3),$$

where AOD(λ)/AOD(870) is the ratio of AOD at specified λ over that at λ=870nm.

The parametrization of cloud effect on actinic flux is according to (Hu and Stamnes, 1993) to convert the cloud microphysical properties to optical properties. The inputs used are the in-situ measured vertical profiles of LWC, and cloud cover set as 0.15 according to the aircraft camera (Fig. S5). For details of the settings for the radiative transfer calculation refer to Table S1.

The absorption power of BC is then calculated as the actinic flux multiplied by absorption coefficient integrated over all λ and BC core sizes, expressed in Equation (4):

$$P_{abs} = \int_{D_c=50nm}^{800nm} \int_{\lambda=250nm}^{2550nm} F_{ac}(\lambda)\, \sigma_{abs,rBC}(\lambda, D_c) M_{rBC}(D_c) d\lambda dD_c \quad (4),$$

where $\sigma_{abs,rBC}$ is the BC mass absorption cross section (in $m^2\ g^{-1}$), which is a function of incident λ and BC core size (D_c), M_{rBC} is the rBC mass concentration at each D_c bin (in $\mu g\ m^{-3}$), multiplying both to obtain the absorption coefficient of rBC (in Mm^{-1}), and the actinic flux (F_{ac}, in mWm^{-2}) is calculated from the DISORT radiative transfer module. Integrating over all wavelengths (λ=250-2550nm) and D_c range (50-800nm) gives the BC absorption power in unit volume of air (in $mW\ m^{-3}$). The absorption power deposition efficiency (P_{eff}) is the P_{abs} normalized by rBC mass in mW/(μg rBC).

3. Results

Fig. 2 schematically shows the mechanism this study will illustrate, which is the enhanced heating rate of BC above the PBL, resulting from combined effects of enhanced secondary formation, BC coatings and cloud reflection on actinic flux at this layer. These are in detail discussed in the following. For guidance, besides main figures, in the supplement, Fig. S1 and S2 shows the temporal evolution of wind profiles and aerosol extinction respectively; Fig. S3 shows MODIS cloud and AOD images; Fig. S4 shows measured typical size distribution; Fig. S5, S6 shows the vertical profiles of meteorological parameters, particle number concentrations and BC-related properties, respectively.

3.1 Meteorology

The flights from 13th-15th July followed very close to the same route (Fig. 1a). The flight region was about 200km away from the coast of the East Ocean and is influenced by sea-land breezes in summertime. The top of PBL could be determined by the aircraft in-situ measured temperature inversion and stable potential temperature (Fig. S5), with the dash lines showing the height of the

PBL (PBLH). Radar wind profiles (Fig. S1) showed diurnal variation of wind shear which also reflected the PBLH. In the PBL the oceanic easterly air flow dominated, and above the PBL was continental southwesterly airmass. The PBLH increased from ~0.5km to ~1.1-1.5km from morning to early afternoon due to stronger convective mixing through daytime surface heating. At night the height of wind shear top was significantly lowered to be ~200m, consistent with the aircraft in-situ measured shallow temperature inversion for the post-sunset flight (Fig. S5). The high pressure centred over the East Ocean, evident in the 700hpa geopotential height (Fig. 1c), led to southwesterly continental transport to the flight location. During all three flight days the synoptic condition maintained a similar pattern. The backtrajectory analysis (Fig. 1a) showed that the measured air masses were transported about 50km (0.2º in latitude) from the south to the flight region in three hours. The region within this distance was controlled by a similar synoptic system (Fig. 1c). This means the air masses observed at different time of the day (in 3 hours transport) could be generally deemed to have similar air mass origin and regional influence. The Beijing winter and summer campaigns also chose the flights without important regional transport or shift of sources, e.g. the variation of rBC mass loading was less than 20% in the lower free troposphere (Fig. S7), and the variation of rBC mass in the PBL was due to daytime boundary layer development when some rBC mass from ground sources could be transported upwards to higher level. The atmospheric processing is thus considered to be mainly at local scale for the results here.

Persistent cloud layers were observed in 0714 and 0715 during Xuzhou campaign, principally thin layers of cumulus humilis, with cloud coverage of about 15-25% according to the aircraft camera and MODIS visible cloud images (Fig. S3). The FCDP-measured LWC (Fig. S5) indicates the location of cloud layer. The presence of these layers may partly reduce the visibility of MODIS AOD data on 0714 and 0715 (Fig. S3), whereas on 0713 the cloud was not as intense thus AOD data is fully visible.

3.2 Enhanced heating rate of BC above the PBL in early afternoon

Fig. S6 shows the vertical profiles of aerosol number concentration for both Aitken and accumulate mode particle, PM1 mass concentration and effective diameter (D_{eff}) at 120-800nm. Note that on 0713 the daytime profiles were from morning (9am) to midday (11:30am), whereas on 0714 and 0715 they were from midday (12:00pm) to early afternoon (14:30pm). The development of the PBL led to uplifting of aerosol from the surface, coming with some dilution effect for certain days, i.e. reduced surface concentration. The residue layer was observed at night above the shallow inversion layer (not on 0715 as no observed inversion). On 0714 and 0715 there were notable increases in PM1 by a factor

of 3-5 above the PBL (Fig. S4c), which occurred in 2-3 hours from midday to early afternoon. This came with a decrease of Aitken mode particle number concentration (Fig. S6a) and considerably increased particle size (Fig. S6d) by 20%. This increase of particulate mass was less pronounced on 0713 when profiles were conducted from morning to midday. This phenomenon was further validated by two lidar measurements away from the flight area with distance of about 170km and 270km respectively. As Fig. S2 showed, the extinction profile from lidar measurements at both locations featured with a fast developed PBL from 12:00 to 15:00, in addition there was an aerosol layer formed above the PBL during this time. This wide spatial consistency confirmed the regional nature of this phenomenon. Given this growth occurred during the period when solar radiation is most intense, it is inferred that aerosol growth within this layer may be driven by photochemical processing of gaseous precursors.

Fig. 3a showed that there was no notable variation of rBC mass above the PBL from 12:00 to 14:30 in both 0714 and 0715. The change in total particulate mass (PM1) normalized by the rBC mass could broadly reflect the formation of secondary aerosol mass, because rBC is always primary while the addition of extra PM1 mass will be mainly controlled by secondary formation (assuming the variation in the relative emission factors of other species is not significant in this relatively short experimental period). The consistent PM1/BC ratio in the PBL (Fig. 3b) at different times of the day suggested well-mixed primary and secondary sources, whereas a remarkable increase of PM1/rBC occurred above the PBL from midday to early afternoon by a factor of 3-5, and this was also consistent with the lidar-measured extinction across the region (Fig. S2).

The coatings associated with rBC, indicated by the coating/rBC mass ratio (Fig. 3c), also increased by a factor of 3-5 similar to PM1/rBC from midday to early afternoon. The absorption efficiency of BC and the absorption enhancement relative to uncoated BC increased from 5% up to 50% (Fig. 3d). Both 0714 and 0715 showed consistent results whereas in 0713 this enhancement was not observed (Fig. S7) as the measurements were from morning to midday. The PM1/rBC and the coatings of BC above the PBL at night decreased compared to that in the early afternoon, consistent with the lidar extinction, and this in turn suggested the importance of solar radiation on the formation of secondary aerosol. There was an increase of RH from 60% to 70% on 0714 between profiles in midday and early afternoon, which was more likely from the moisture uplift through convective mixing as there was no obvious wind profile (Fig. 1) or air mass shift (according to backtrajectory analysis). This may cause more significant increase of PM1 and particle size (Fig. S6) compared to that on 0715, because more water molecular could also promote photochemical reactions and allow more semi-volatile species to condense (Donahue et al., 2006). There was no obvious variation of RH on 0715

but still showed significant enhancement of secondary species, for which the sole photochemical reaction tended to dominate. There was no solar irradiance increase from morning to midday on 0713 thus no obvious secondary species formed. The results over Beijing in summer ((Zhao et al., 2019), Fig. 2) also confirmed the strong enhancement of BC coatings above the PBL in 2-3 hours evolution time by a factor of 2-3 occurring in the early afternoon, however was at a lower scale compared to Xuzhou, and this may result from a drier air mass (RH<60%, Fig. S5) in the FT for northern cities; whereas in Beijing winter this enhancement was significantly reduced with coating enhancement less than a factor of 1.5 or even decreased from midday to early afternoon (Fig. 4), which may be due to the reduced solar radiation and enhanced AOD dimming effect in winter (given the winter flights were conducted during a heavily polluted period with surface rBC mass loading >4μg m^{-3}). A recent study conducted over Korea (Lamb et al., 2018) also indicated some enhanced coating thickness of BC above the PBL (in Fig. 4b at about 800hpa compared to 100hpa), whereas the mixing state of BC at higher altitude was more influenced by synoptic conditions. The enhanced coating of BC above the boundary layer therefore tends to be a general phenomenon for the site where intensive solar radiation is received above the PBL.

The observations here showed strong enhancements for secondary formation, BC coatings and absorption above the PBL in the hours with most intense solar radiation, however these enhancements were less pronounced in the PBL. This could be caused by strong photochemical activities above the PBL, while the increased aerosol optical depth may have a significant optical shielding effect in the PBL (Prabha and Hoogenboom, 2009; Streets et al., 2006). Radiative transfer calculations (Fig. S9) show that direct solar irradiance was reduced, especially within the PBL, by adding the measured aerosol loadings, whereas the downward diffuse irradiance was enhanced above the PBL due to increased particle size. The overall actinic flux thus showed significant enhancement above the PBL, compared to within the PBL, due to the aerosol loading (especially for the early afternoon in 0714 and 0715). As Fig. 3b shows, the absolute absorbing power of BC was largely determined by the rBC mass loading, with heating rate 0.3-0.5 K/d in the PBL, while 0.1-0.18 K/d above the PBL. The power deposition efficiency (P_{eff}, as normalized by rBC mass) depended on the absorption efficiency of BC (MAC). In the PBL, the clear-sky P_{eff} 6-8mW/(μg rBC) was broadly within that measured in a North American city 7±2.5mW/(μg rBC) (Schwarz et al., 2009). Corresponding with the increase of BC coatings from midday to early afternoon, the P_{eff} showed an enhancement of up to 30% from ~7.0 to 9.5 mW/(μg rBC) above the PBL from midday to early afternoon.

The presence of cloud layers above the PBL further altered the irradiance, i.e. enhancing the dimming at lower level but increasing the reflectance above the cloud layer (Fig. 5a). The thin cloud layer in

this study was mainly cumulus humilis with 15-25% cloud cover and LWC 0.1-0.3 g m^{-3}. The cloud layer enhanced the F_{ac} above the PBL by 30% but weakened the F_{ac} below the PBL by 15%. This study finds the P_{eff} above the PBL will be further enhanced by 10% if considering the cloud coverage of 15% (Fig. 5c). Note that the cloud fraction is only an approximate estimate here but the F_{ac} will be further amplified if more cloud coverage. The absorption enhancement due to cloud reflection was previously studied for the BC above oceanic stratocumulus (Johnson et al., 2004) but this study provides the direct evidence. It should be also noted that the patchy nature of the cloud layer (Fig. S3 and S5) may have allowed aerosols or precursors to penetrate the cloud layer, in order to form a BC layer with significant secondary coatings above the cloud layer, which may explain the cases for this study.

4. Discussion and Conclusion

In this study, the fast formation of a secondary aerosol layer was observed during summertime: within three hours from midday to early afternoon, the contribution of secondary aerosol above the planetary boundary layer (PBL) increased by a factor of 3-5. This is likely due to the higher rates of photochemical processing at these altitudes, which is suppressed in the PBL due to dimming caused by the high AOD. The secondary species formed by this processing will condense on the BC and increase its coating content, leading to an enhancement of absorption efficiency by 50%. Consequently, the absorbing power deposited on the BC will be enhanced by combined effects of increased coatings and solar flux. These processes are schematically illustrated in Fig. 2. The results here are consistent with the chamber simulation study by (Peng et al., 2016) that a BC E_{abs} of ~50% occurred in 2-3 hours' ageing time during pollution condition. In addition, the solar flux received above the PBL as in this study may be more intensive than that on the ground because of less AOD dimming effect in addition to the cloud reflection above the PBL.

Cloud layers regularly form on top of the PBL in this region, and strong solar reflection by cloud top will significantly increase the actinic flux received by the BC above the cloud layer, further amplifying the amount of solar radiation absorbed by the BC. Given the strong solar radiation in summertime, all of these processes will occur in a short time scale. This strong heating effect of BC introduced by combining processes (intensive solar radiation, secondary coatings and cloud reflection) would considerably increase the temperature above the PBL, which may introduce feedback effects and accumulate more pollutants across this layer, further promoting the secondary formation. Previous study found the absorbing aerosols above the cloud may stabilize the underlying layer and

290 tend to enhance the cloud coverage below (Brioude et al., 2009), which may in turn enhance this
291 feedback. This mechanism raised in this study should be considered when evaluating the BC heating
292 effect at polluted region rich in BC and precursors, especially in summertime when solar radiation is
293 strong. Further chemical measurements in gas and aerosol phase are also needed to elucidate the
294 complex interactions over the top of the PBL.

295

Figures and captions

(a) (b)

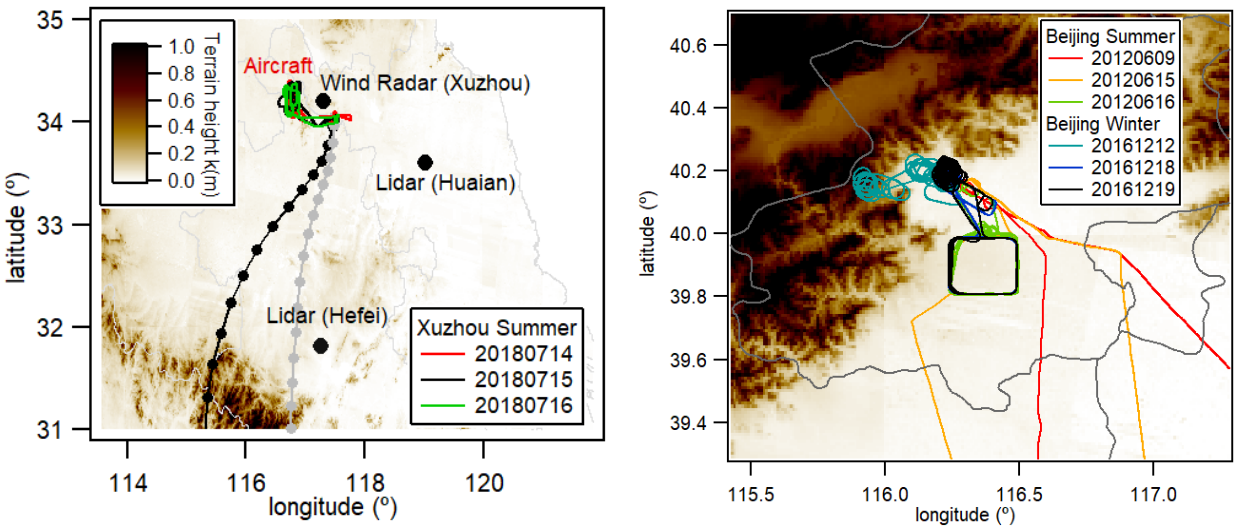

(c)

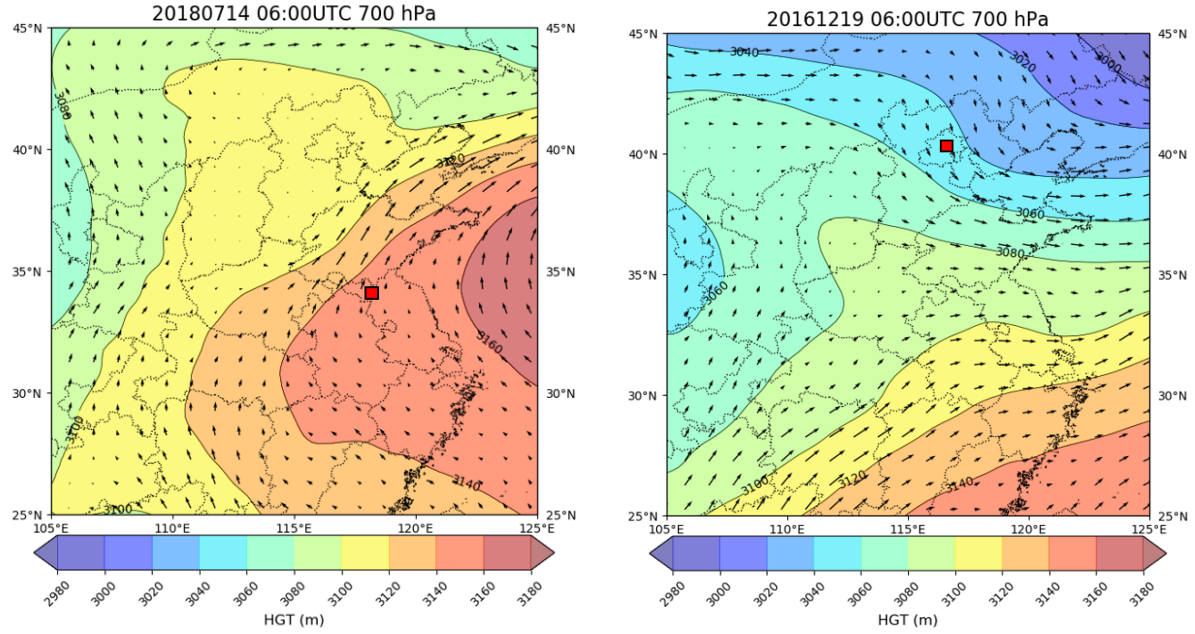

Fig. 1. (a) Flight tracks (coloured by aircraft altitude), locations of lidars in Huaian and Hefei, and wind profile radar in Xuzhou (indicated by black dots). The black and grey lines show the backtrajectories initialized at altitudes of 1.5km (above the PBL) and 0.5km (in the PBL) respectively, each dot indicating a 1h time interval. (b) Flight tracks for Beijing 2012 summer and 2016 winter campaigns. c) geopotential height in the free troposphere (at 700hpa) for Xuzhou and Beijing, the red marker on each plot indicates the location of profiles.

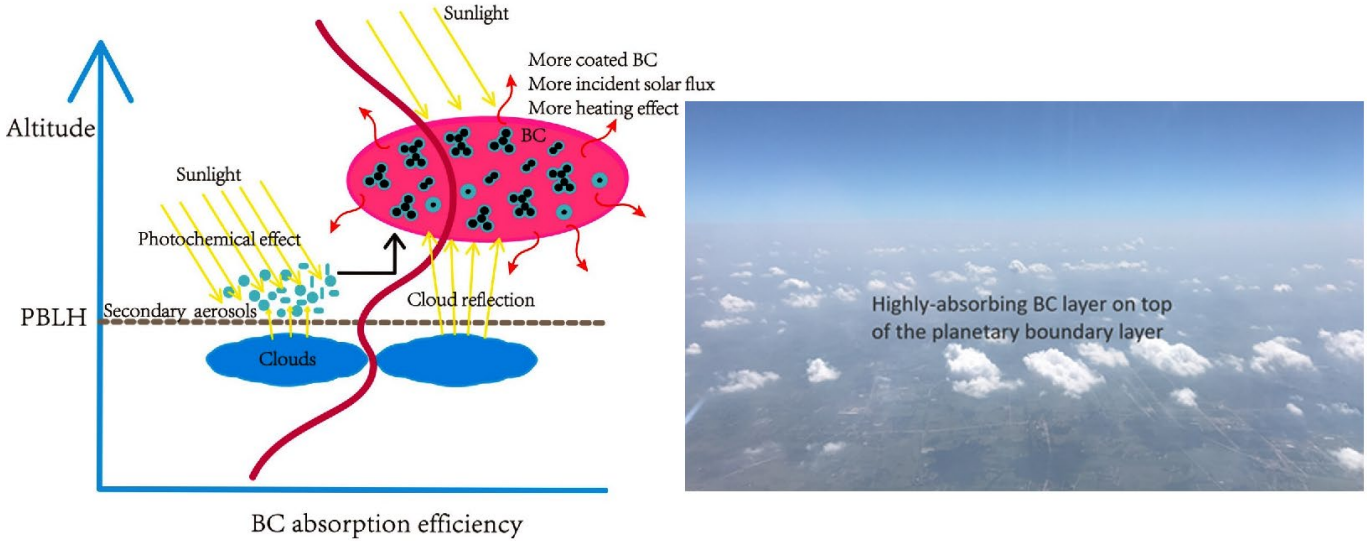

Fig. 2. Schematics and image illustrating the enhancement of BC heating effect above the PBL, resulting from the combined effects of enhanced secondary formation, BC coatings and cloud reflection above the PBL.

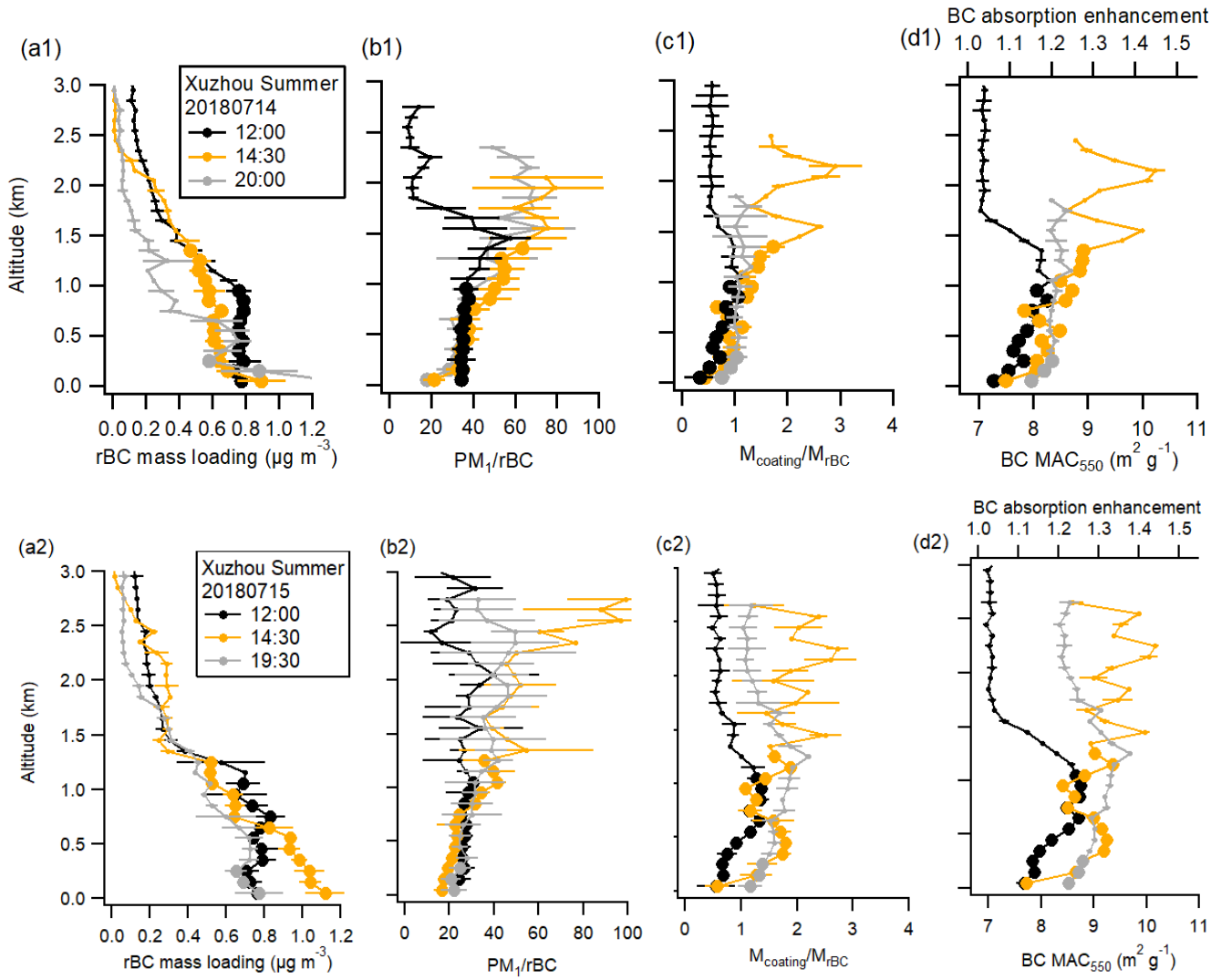

Fig. 3. Vertical profiles of BC-related properties during Xuzhou summer campaign. (a) rBC mass loading, (b) mass ratio of PM1/rBC, (c) mass ratio of coating/rBC ($M_{coating}/M_{rBC}$), and (d) BC mass absorption cross section (MAC_{550}) and absorption enhancement all profiles in 0714 and 0715. The dash lines show the PBLH for each profile. The lines and error bars show mean±σ at each altitude bin. The large and small markers denote the planetary boundary layer (PBL) and free troposphere (FT) respectively.

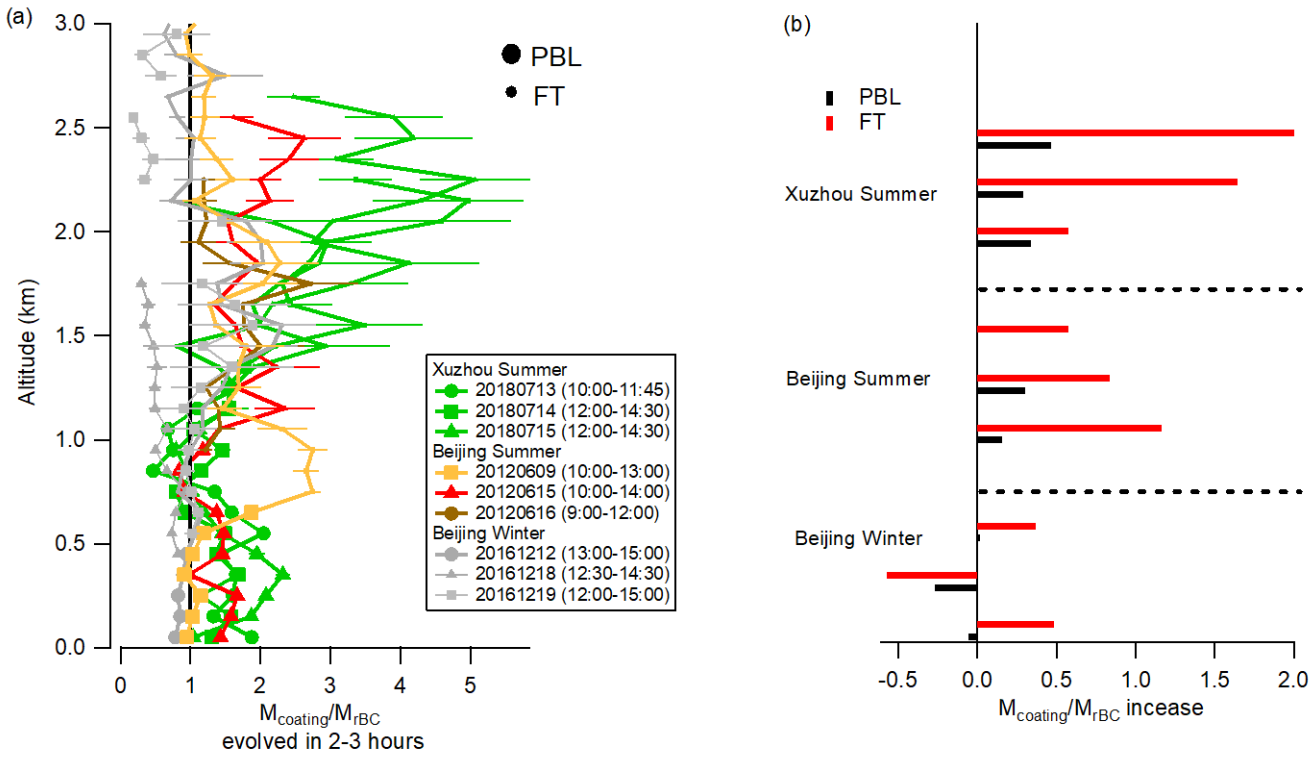

Fig. 4. The ratio of $M_{coating}/M_{rBC}$ in 2-3 hours processing (return profile divided by departure profile) for Xuzhou 2018 summer, Beijing 2016 winter and 2012 summer campaigns in (a). The large markers denote the PBL. The time in bracket denote the time of departure and return profiles for each flight. (b) shows the mean increase of $M_{coating}/M_{rBC}$ in the PBL and FT respectively, deducted from the results shown in (a).

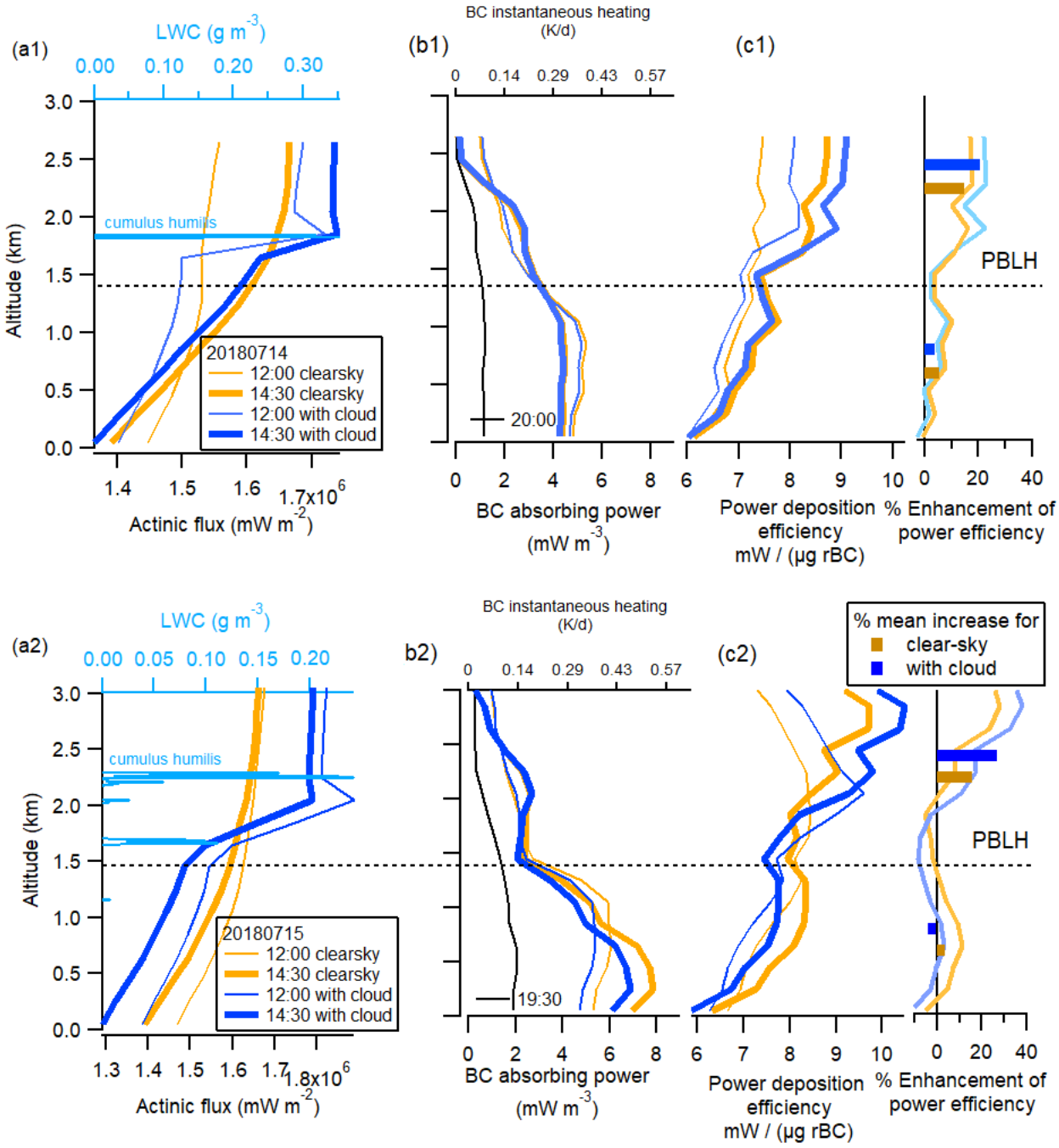

Fig. 5. The radiative transfer results during Xuzhou summer campaign. (a) actinic flux in the midday and early afternoon with and without cloud (the night flux is $<10^6$ mW m^{-2}), with the blue lines showing the FCDP-measured LWC. (b) BC absorbing power and instantaneous heating rate. (c) Power efficiency deposited on BC, and its increasing rate in percentage from midday to early afternoon. The dash lines show the height of planetary boundary layer (PBLH). The bars on the right panels show the mean % enhancement of power efficiency within and above the PBL for clear-sky and with-cloud conditions respectively.

Acknowledgment

This research was supported by the National Key Research and Development Program of China (2016YFA0602001), National Natural Science Foundation of China (41605108, 41875167, 41875044, 41505128, 41505129, 41775138, 41807313). Processed data is downloadable from the link (https://pan.baidu.com/s/1NgHxiBcPKUeSNeJVoFmsbQ) by using extracting code 57wX.

References

Babu, S. S., et al., 2002. Aerosol radiative forcing due to enhanced black carbon at an urban site in India. Geophysical Research Letters. 29**,** 27-1-27-4.

Bond, T. C., Bergstrom, R. W., 2006. Light absorption by carbonaceous particles: An investigative review. Aerosol science and technology. 40**,** 27-67.

Brioude, J., et al., 2009. Effect of biomass burning on marine stratocumulus clouds off the California coast. Atmospheric Chemistry and Physics. 9**,** 8841-8856.

Cross, E. S., et al., 2007. Laboratory and ambient particle density determinations using light scattering in conjunction with aerosol mass spectrometry. Aerosol science and technology. 41**,** 343-359.

Ding, A., et al., 2016. Enhanced haze pollution by black carbon in megacities in China. Geophysical Research Letters. 43**,** 2873-2879.

Donahue, N., et al., 2006. Coupled partitioning, dilution, and chemical aging of semivolatile organics. Environmental Science & Technology. 40**,** 2635-2643.

Draxler, R. R., Hess, G., 1998. An overview of the HYSPLIT_4 modelling system for trajectories. Australian Meteorological Magazine. 47**,** 295-308.

Emde, C., et al., 2016. The libRadtran software package for radiative transfer calculations (version 2.0. 1). Geoscientific Model Development. 9**,** 1647-1672.

Hu, Y., Stamnes, K., 1993. An accurate parameterization of the radiative properties of water clouds suitable for use in climate models. Journal of climate. 6**,** 728-742.

Jacobson, M. Z., 2012. Investigating cloud absorption effects: Global absorption properties of black carbon, tar balls, and soil dust in clouds and aerosols. Journal of Geophysical Research: Atmospheres. 117.

Johnson, B. T., et al., 2004. The semi-direct aerosol effect: Impact of absorbing aerosols on marine stratocumulus. Quarterly Journal of the Royal Meteorological Society. 130**,** 1407-1422.

Koch, D., Del Genio, A., 2010. Black carbon semi-direct effects on cloud cover: review and synthesis. Atmospheric Chemistry and Physics. 10**,** 7685-7696.

Lamb, K. D., et al., 2018. Estimating Source Region Influences on Black Carbon Abundance, Microphysics, and Radiative Effect Observed Over South Korea. Journal of Geophysical Research: Atmospheres. 123.

Liu, D., et al., 2014. Size distribution, mixing state and source apportionment of black carbon aerosol in London during wintertime. Atmospheric Chemistry and Physics. 14**,** 10061-10084.

Liu, D., et al., 2015. The effect of complex black carbon microphysics on the determination of the optical properties of brown carbon. Geophysical Research Letters. 42**,** 613-619.

Liu, D., et al., 2017. Black-carbon absorption enhancement in the atmosphere determined by particle mixing state. Nature Geoscience. 10**,** 184-188.

Liu, Q., et al., 2018. A study of elevated pollution layer over the North China Plain using aircraft measurements. Atmospheric Environment. 190**,** 188-194.

Nenes, A., et al., 2002. Black carbon radiative heating effects on cloud microphysics and implications for the

aerosol indirect effect 2. Cloud microphysics. Journal of Geophysical Research: Atmospheres. 107.
Norris, J. R., Wild, M., 2009. Trends in aerosol radiative effects over China and Japan inferred from observed cloud cover, solar “dimming,” and solar “brightening”. Journal of Geophysical Research: Atmospheres. 114.
O’Connor, D., et al., Upgrades to the FSSP-100 electronics. International Conference on Clouds and Precipitation, Cancun, Mexico.[Available at http://convention-center. net/iccp2008/abstracts/Program_on_line/Poster_13/O-Connor_extended_final. pdf, 7–11 July.], 2008.
Peng, J., et al., 2016. Markedly enhanced absorption and direct radiative forcing of black carbon under polluted urban environments. Proceedings of the National Academy of Sciences. 201602310.
Prabha, T. V., Hoogenboom, G., 2009. Observed dimming effect during a forest fire in the southeastern United States and the role of aerosols. Geophysical Research Letters. 36.
Ramanathan, V., Carmichael, G., 2008. Global and regional climate changes due to black carbon. Nature geoscience. 1**,** 221-227.
Schwarz, J., et al., 2006. Single‐particle measurements of midlatitude black carbon and light‐scattering aerosols from the boundary layer to the lower stratosphere. Journal of Geophysical Research: Atmospheres (1984–2012). 111.
Schwarz, J. P., et al., 2009. Heating rates and surface dimming due to black carbon aerosol absorption associated with a major U.S. city. Geophysical Research Letters. 36**,** n/a-n/a.
Streets, D. G., et al., 2006. Two‐decadal aerosol trends as a likely explanation of the global dimming/brightening transition. Geophysical Research Letters. 33.
Ting, Y., et al., 2018. The Mixing State of Carbonaceous Aerosols of Primary Emissions from 'Improved' African Cookstoves. Environ Sci Technol.
Zhao, D., et al., 2019. Vertical characteristics of black carbon physical properties over Beijing region in warm and cold seasons. Atmospheric Environment.
Zhao, D., et al., 2015. In-situ aircraft measurements of the vertical distribution of black carbon in the lower troposphere of Beijing, China, in the Spring and Summer Time. Atmosphere. 6**,** 713-731.